Astronomy & Astrophysics manuscript no. September 25, 2002
(DOI: will be inserted by hand later)

Far-infrared photometry of deeply embedded outflow sources⋆

Dirk Froebrich[1], Michael D. Smith[2], Klaus W. Hodapp[3] and Jochen Eislöffel[1]

[1] Thüringer Landessternwarte Tautenburg, Sternwarte 5, D-07778 Tautenburg, Germany
[2] Armagh Observatory, College Hill, Armagh BT61 9DG, Northern Ireland
[3] University of Hawaii, Institute for Astronomy, 640 N. Aohoku Place, Hilo, HI 96720, USA

Received sooner / Accepted later

Abstract. We present far-infrared maps and spectroscopy for several deeply embedded protostellar objects from data acquired with the ISO instruments PHOT and LWS. Spectral energy distributions for Cep E, HH 211-MM, IC 1396 W, L 1157, L 1211 and RNO 15 FIR indicate that these are relatively cold Class 0 sources. Several previously undetected deeply embedded sources are found in the vicinity of our targets. We determine temperatures and luminosities of seven objects and locate them on a L_{bol}-T_{bol} diagram – the equivalent to a Hertzsprung-Russell diagram for protostars. Their masses and ages, according to their location on tracks derived from an/our evolutionary model, are derived. L 1211 and Cep E appear to be intermediate mass objects which will reach final masses of about 3 $M_{\odot}$, while the other sources are in or below the solar mass range. The derived ages of 15000 to 30000 yr are consistent with their current Class 0 state. A comparison of the luminosity of the associated outflows in the 1 – 0 S(1) line of molecular hydrogen with the source properties (bolometric luminosity, bolometric temperature and envelope mass) of 15 Class 0 sources shows no statistically significant correlations. Nevertheless, the data are consistent with a scheme in which the outflow strength and protostar evolve simultaneously. The relationship is partially disguised, however, by the local properties of the surrounding material, the extinction and short-term flux variability.

Key words. Stars: evolution – Stars: formation – Infrared: stars

1. Introduction

In the earliest stages of star formation – the so-called Class 0 and Class 1 phases – protostars are still deeply embedded in their parental molecular cloud cores. This material absorbs almost all of the emitted radiation of the star in the optical and the near-infrared. The spectral energy distribution (SED) of Class 0 protostars therefore peaks at about 40–100 μm, the wavelength of the maximum of a blackbody at 30–80 K. Hence, direct observations of protostars have to be carried out in the far-infrared and in the (sub-)mm wavelength range. Sub-mm and millimeter observations of some of the sources investigated here have been carried out e.g. by Lefbch et al. (1996), Ladd & Hodapp (1997), Chini et al. (2001), Gueth et al. (1997), Motte & André (2001) and Gueth & Guilloteau (1999).

The ISO satellite (Kessler et al. 1996) with its PHOT instrument had the capacity to measure the broad-band continuum in the far-infrared. Such observations, covering the peak region of the SED of protostars, help to yield some of the major properties of these objects such as their temperature, the sub-mm slope of their SED, the optical depth and the solid angle under which they emit. The latter two cannot be disentangled due to the limited spatial resolution of the ISOPHOT instrument. With higher resolution observations, however, (e.g. SCUBA) we can determine the solid angle under which an object is seen independently and that way infer its optical depth. These parameters, together with the distance, enable us to calculate the total (L_{bol}) and sub-mm (L_{smm}) luminosities of each object. We may then decide whether an object really is of Class 0 or not by determining the L_{smm}/L_{bol} ratio (André et al. 2000). Finally, by placing the inferred values on a temperature – bolometric luminosity diagram – the equivalent to a Hertzsprung-Russell diagram for protostars (Myers et al. 1998) – we are able for the fi rst time to determine the (model dependent) ages and masses of these sources directly.

Bipolar outfbws invariably accompany Class 0 sources: strong infbw and outfbw of material are concurrent. We thus wish to probe how the mass outfbw rate is related to the mass accretion rate onto the protostar. The outfbwing material interacts with the ambient medium through radiative shocks. Thus, the luminosity of the outfbw may be correlated with some of the source properties (e.g. the bolometric source luminosity), which depend on the mass accretion rate. Therefore, we measured the luminosities of the outfbws of 15 Class 0 sources in the 1 – 0 S(1) line of molecular hydrogen. This is usually the strongest and easiest line to observe in near-infrared spectra of shocked molecular hydrogen, and due to the short cooling time

Send offprint requests to: Dirk Froebrich

⋆ Based on observations with ISO, an ESA project with instruments funded by ESA Member States (especially the PI countries: France, Germany, the Netherlands and the United Kingdom) and with the participation of ISAS and NASA.

Table 1. Log of our ISOPHOT and LWS observations.

Observation number	Object	α (J2000)	δ (J2000)	AOT	t_{exp} [s]
65903003	RNO 15 FIR	03 27 39	+30 13 00	PHT22	670
65903004	RNO 15 FIR	03 27 39	+30 13 00	PHT22	620
65903101	HH 211	03 43 57	+32 00 49	PHT22	670
65903102	HH 211	03 43 57	+32 00 49	PHT22	620
65201107	HH 211	03 43 57	+32 00 52	LWS01	2268
65902801	HH 211 West	03 43 57	+32 01 04	LWS01	3350
66600502	HH 211 East	03 43 59	+32 00 36	LWS01	2912
46601429	L 1157	20 39 06	+68 02 13	LWS01	3390
28200120	L 1157	20 39 06	+68 02 14	LWS01	1958
52902105	L 1157	20 39 06	+68 02 14	PHT22	668
52902106	L 1157	20 39 06	+68 02 14	PHT22	620
54301407	IC 1396W	21 26 06	+57 56 17	PHT22	668
54301408	IC 1396W	21 26 06	+57 56 17	PHT22	620
56300709	L 1211	22 47 17	+62 01 58	PHT22	670
56300710	L 1211	22 47 17	+62 01 58	PHT22	620
56600912	Cep E South	23 03 13	+61 41 56	LWS01	1888
56402111	Cep E	23 03 13	+61 42 27	PHT22	670
56402112	Cep E	23 03 13	+61 42 27	PHT22	620
56601113	Cep E North	23 03 13	+61 42 59	LWS01	1890

of H_2 it is a good tracer of the present interaction of the outflow with the surrounding material. These H_2 luminosities are then compared with various source properties to investigate possible correlations.

Modelling of Class 0 protostars remains in its infancy. Schemes now exist which yield evolutionary tracks, based on relating gas accretion to the dusty envelope (Myers et al.1998) and jet thrust to gas accretion (Bontemps et al. 1995, Saraceno et al. 1996, Smith 1999, 2000 and André 2000). We combine these schemes here in order to test if the simplest assumptions, such as a spherical envelope and a single accreting object, are feasible.

In this paper, we first present our far-infrared ISO maps and spectroscopy, and then summarize the data analysis and how we derive temperatures and luminosities (Sect. 2). In Sect. 3, we present our results, and comment on individual objects. A discussion of age and mass determination, and the general relatioship to the outflows is contained in Sect. 4. A framework within which the data can be interpreted is then put forward (Sect. 5).

2. Observations and Data Analysis

We used the ISO satellite to obtain ISOPHOT minimaps of six Class 0 sources and LWS full grating spectra for three of them. All observations are listed in Table 1.

2.1. ISOPHOT data

Minimaps were taken for six objects (Cep E, HH 211-MM, IC 1396 W, L 1157, L 1211 and RNO 15 FIR) with ISOPHOT in its PHT22 mode by single pointing and moving of the telescope by one (C100) or half (C200) of a detector pixel. We used four filters (60, 100, 160 and 200 μm). For 60 and 100 μm, the C100 detector (3×3 array of Ge:Ga) was used to create a 5×3 pixel minimap with a pixel size of $45'' \times 46''$. The maps thus cover a field of view of $230' \times 135''$. For the two longer wavelengths 7×3 mosaics with a pixel size of $45'' \times 90''$ were obtained using the C200 detector (2×2 array of stressed Ge:Ga), covering thus a field of view of $315'' \times 270''$. For details on the instrument and the used Astronomical Observing Templates (AOT) see the ISO Handbook, Volume V: PHT — The Imaging Photo Polarimeter[1] and Lemke et al. (1996). The data were reduced with the ISOPHOT Interactive Analysis (PIA V9.1) software.

Flux measurements in the ISOPHOT maps were carried out in two different ways: 1) Point spread function (PSF) photometry using PSF fractions provided by Laureijs (1999) was done for the C100 maps. We do not provide PSF photometry for the C200 detector since the given PSF fractions by Laureijs (1999) are only for the whole C200 pixel and our maps have a sampling of half a pixel in one direction. 2) "Aperture" photometry was obtained for all filters of both C100 and C200 detectors. Here we attributed each pixel in the maps either to 'object' or to 'background' manually, then summed up both and subtracted 'background' from 'object' to obtain its flux. Since at 60 and 100 μm, i.e. for the C100 data, we were able to do photometry with both methods, we have a means of estimating the consistency of both. All measured fluxes, including the available IRAS fluxes of our objects, and the background level in the maps are provided in Table 3.

Table 2. Observation log of the NIR observations. The used telescopes, detectors and filters are listed. H_2 indicates the narrow line filter, centered at the 1–0 S(1) line of H_2. The narrow band filter at a wavelength of 2.140 μm (continuum) is labeled with 2140. The number of pictures is separately indicated for each filter. In some cases the investigated objects fill only a part of the whole obtained mosaic (esp. HH 212). The observing time is given per single image.

Observatory Date	Telescope Detector	Object	Filter	Number of images	t_{obs} (s)
La Silla Apr93	ESO/MPI 2.2-m IRAC2	HH 24	H_2, K'	12, 3	20, 2
		Ser – FIRS1	H_2, K'	23, 4	20, 2
		VLA 1623	H_2, K'	24, 4	20, 2
Calar Alto Jan94	2.2 m MAGIC	L 1448	H_2, K'	32, 33	60, 3
Calar Alto Sep94	2.2 m MAGIC	DR 21	H_2, K'	437, 78	25, 25
		L 1157	H_2, K'	140, 13	25, 100
Calar Alto Nov95	3.5 m MAGIC	Cep E	H_2, 2140	52, 120	30, 30
		HH 211-MM	H_2, 2140	60, 59	30, 30
		L 1157	H_2, 2140	44, 71	30, 30
Mauna Kea Aug97	UH 2.2-m QUIRC	L 1211	H_2, K'	28, 27	200, 60
Calar Alto Sep97	3.5 m MAGIC	Cep A	H_2, 2140	202, 368	20, 20
		HH 211	H_2, 2140	32, 27	20, 20
		L 1448	H_2, K'	247, 253	20, 3
Calar Alto Nov98	1.2 m MAGIC	Cep A	H_2, K'	64, 32	60, 15
		Cep E	H_2, K'	34, 14	60, 15
		HH 212	H_2, K'	3112, 1487	60, 15
		L 1448	H_2, K'	400, 149	60, 15
		RNO 15 FIR	H_2, K'	120, 60	60, 15
Calar Alto Dec00	3.5 m OMEGA PRIME	Cep E	H_2	24	30
		HH 211	H_2	41	30
		L 1157	H_2	17	30
		L 1448	H_2	42	30

2.2. LWS data

For three objects (L 1157, Cep E and HH 211) we have full grating medium-resolution LWS01 scans, which cover a wave-

[1] http://www.iso.vilspa.esa.es/manuals/HANDBOOK/V/pht_hb/

length range from 43 to 196.9 μm with a resolving power between 150 and 300. See the ISO Handbook, Volume IV: LWS — The Long Wavelength Spectrometer[2] and Clegg et al. (1996) for instruments and AOT details. We reduced the LWS data using standard pipeline 7. For deglitching and flux calibration and defringing of the spectra we employed the ISO Spectral Analyses Package (ISAP 1.6a).

2.3. Near-infrared H_2 observations

For the measurement of the luminosities of the outflows in the 1 – 0 S(1) line of molecular hydrogen at 2.122 μm near-infrared images were taken in several observing campaigns and at various telescopes. The complete list of all observations is provided in Table 2. We observed the objects in two filters to distinguish between line and continuum emission. Due to the angular size of the objects, the single images had to be arranged into large mosaics. This was done using the IRAF package DIMSUM. The whole procedure includes flatfielding, cosmic ray hit removal and sky subtraction as well as re-centering and mosaicing. For a higher astrometric accuracy we used all available stars in the field for the re-centering. The photometric calibration was achieved by the observation of faint near-infrared standards with an accuracy of 10%. For the flux measurements we subtracted the scaled continuum image from the emission line image to measure only the flux in the 1 – 0 S(1) line of H_2.

2.4. Determination of T_{bol} and L_{bol}

The observed broad-band continuum fluxes of our sources allow us to fit a spectral energy distribution to the measurements and so to infer source properties (e.g. bolometric luminosity and temperature). To fit the spectral energy distribution we used the following equation for the flux density S of our objects:

$$S[Jy] / \Sigma\Omega = \left(1 - e^{-\tau}\right) \cdot B(\lambda, T), \quad (1)$$

where $B(\lambda, T)$ is the Planck function, $\Sigma\Omega$ the solid angle of the source and τ the optical depth. τ is set as

$$\tau = \tau_{100} \cdot \left(\frac{\lambda}{100\mu m}\right)^{-\beta} \quad (2)$$

where λ is in μm, the optical depth at 100 μm (τ_{100}) is a free parameter, and β is the sub-millimeter slope of the spectral energy distributio. The lowest rms of the fit is obtained when the solid angle of the object is determined by

$$\Sigma\Omega = \sum_f \frac{(S_f/\Sigma\Omega) S_f^m}{(\Delta S_f^m)^2} \Bigg/ \sum_f \frac{(S_f/\Sigma\Omega)^2}{(\Delta S_f^m)^2} \ , \quad (3)$$

where f indicates the various used filters, S_f^m the flux measurements in these filters, ΔS_f^m the error of the measurements. $S_f/\Sigma\Omega$ is determined by

$$S_f/\Sigma\Omega = \frac{\int_{\lambda=0}^{\infty} \left(1 - e^{-\tau}\right) B(\lambda, T)\, T_f(\lambda)\, d\lambda}{\int_{\lambda=0}^{\infty} T_f(\lambda)\, d\lambda} \quad (4)$$

[2] http://www.iso.vilspa.esa.es/manuals/HANDBOOK/IV/lws_hb/

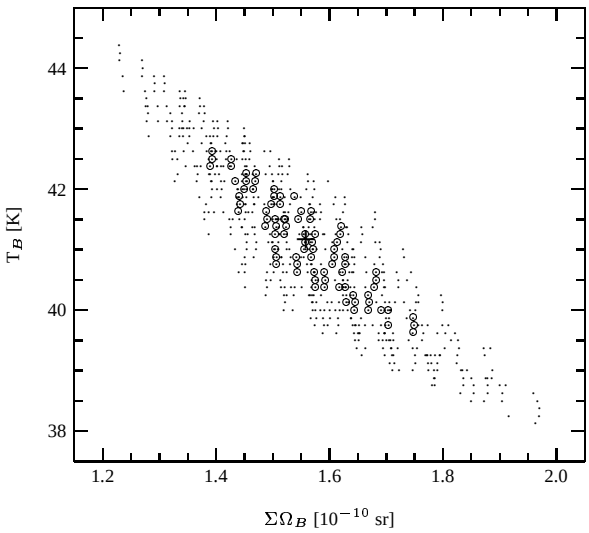

Fig. 1. (T_B,$\Sigma\Omega_B$) plane for the blackbody fit of the Cep E photometry. The fit with the measured fluxes is marked by a cross. Circles indicate fits using fluxes which deviate at most by 0.5 σ, and the small dots represent fits using fluxes with a maximum deviation of 1.0 σ from the measurements.

for each filter f separately using the filter transmission curves $T_f(\lambda)$.

We fit a gray- and a blackbody ($\beta = 0.0$) to the measurements for each object. To do this, we computed a grid of graybodys (see Eq. 1) in which we varied the three parameters temperature, optical depth at 100 μm and sub-millimeter slope of the SED. We varied the temperature between 15 and 80 K, in steps of 0.125 K, the optical depth at 100 μm from 0.09 to 11.4, in logarithmic intervals of 1.5, and the sub-millimeter slope from 0.0 to 3.0, in steps of 0.1. The so determined graybodys were convolved with the filter curves of the four used filter bands (see Eq. 4). Then the solid angle $\Sigma\Omega$ was determined by computing the deviation of the model points from the measurements and minimising this value (see Eq. 3). Finally the rms of the fit to the measurements was determined, scaled by the errors of the measurements, and the parameters leading to the minimal rms were selected. We find that the optical depth has almost no influence on the shape of the graybody curve, but only on the absolute flux level, which on the other hand mainly depends on $\Sigma\Omega$. So, we selected only fits with τ_{100} equal to 1.0. Nevertheless the two parameters $\Sigma\Omega$ and τ_{100} are connected by $\Sigma\Omega^{-1} \propto (1 - e^{-\tau_{100}})$ to first approximation. Thus, the determined values for $\Sigma\Omega$ are only valid under the assumption $\tau_{100} = 1$. If sub-mm or millimetre observations yield other source sizes, the optical depth at 100 μm can be constrained. Note that the size given here is the size of the protostellar envelope where the optical depth at 100 μm is unity. It may differ from the envelope sizes obtained of optically thin emission by sub-mm or millimeter measurements (e.g. Motte & André (2001) and Chini et al. (2001)).

The above described method to fit the SED was first applied only to the measurements at out four ISOPHOT wavelengths. All infered object properties listed in Table 4 are determined using only the ISOPHOT data. In addition, we could extend

Table 3. Far-infrared fluxes for all detected objects, measured with ISOPHOT, and IRAS, as well as SCUBA and IRAM 30-m points from the literature. Columns C_{60}..C_{200} give the fluxes above the background measured with aperture photometry, columns C_{60}^{psf} and C_{100}^{psf} the fluxes obtained by PSF fitting. For comparison we list the IRAS fluxes at 12, 25, 60 and 100 μm in columns I_{12}..I_{100}. S_{450} and S_{850} give SCUBA fluxes at 450 and 850 μm from the literature. I_{1300} is the flux at 1.3 mm. All fluxes are in Jansky. In the B_{60}..B_{200} columns we list the background level in the ISOPHOT maps at 60, 100, 160 and 200 μm in MJy sr^{-1}. The * signs mark the newly detected objects in our maps.

Object	C_{60}	C_{100}	C_{160}	C_{200}	C_{60}^{psf}	C_{100}^{psf}	B_{60}	B_{100}	B_{160}	B_{200}	S_{450}	S_{850}	I_{1300}	I_{12}	I_{25}	I_{60}	I_{100}
RNO 15 FIR	25.7	51.5	46.7	48.9	24.8	55.5	19	25	92	120	9.2	1.4	–	0.25	3.4	47.1	93.6
RNO 15*	3.3	11.9	7.1	10.8	3.7	10.5	19	25	92	120	–	–	–	0.18	4.2	48.8	82.2
HH 211-MM	3.0	33.8	56.2	54.8	1.9	20.8	42	138	308	331	16.4	3.8	0.9	–	–	–	–
HH 211 FIRS2*	2.9	13.7	55.3	48.2	1.0	11.3	42	138	308	331	–	–	–	–	–	–	–
L 1157	6.8	37.8	42.0	38.6	5.9	35.8	11	19	63	72	6.0	0.9	0.4	0.25	0.25	10.9	53.5
IC 1396 W	5.7	19.9	36.6	26.6	4.6	13.8	25	92	210	230	–	–	–	0.25	0.6	9.7	38.3
IC 1396 W FIRS2*	0.1	1.2	33.2	9.9	0.2	1.2	25	92	210	230	–	–	–	–	–	–	–
IC 1396 W FIRS3*	0.1	1.2	4.6	17.3	0.2	2.3	25	92	210	230	–	–	–	–	–	–	–
L 1211	12.9	36.5	63.0	75.0	10.5	23.4	42	157	254	280	–	–	–	2.7	5.7	19.8	63.6(1)
L 1211 FIRS2*	3.4	17.0	31.6	46.2	2.2	10.9	42	157	254	280	–	–	–	–	–	–	–
Cep E	55.2	125.8	102.1	81.4	65.4	123.0	35	99	234	293	43.7	4.1	1.0	0.43	5.8	61.0	112.0

(1) upper limit

Table 4. Best blackbody and graybody fit results (explanation in text), as well as the inferred bolometric and sub-mm luminosities, from our ISOPHOT data points. T_B is the fitted temperature for the blackbody, T_G the temperature of the graybody. For β and $\Sigma\Omega$ see text. The optical depth at 100 μm was fixed to 1.0, since it did not show significant influence on the shape of the graybody curve. The rms gives the error of the fit from the measurements scaled with the errors of the measurements. The explanation of the determination of the errors is given in the text. $\Sigma\Omega$ is given in 1×10^{-10} sr (equal to 4.25 □″). The sub-mm luminosity L_{smm} is the luminosity of the object at wavelengths larger than 350 μm, and the bolometric temperature T_{bol} is the temperature of a blackbody with the same luminosity as the object. The * signs mark newly discovered objects. Due to the photometry problems with these objects, we do not present errors here.

Object	T_B [K]	$\Sigma\Omega_B$	rms_B	T_G [K]	β	$\Sigma\Omega_G$	rms_G	R [pc]	T_{bol} [K]	L_{bol} [$L_\odot$]	L_{smm}/L_{bol}	Class 0
RNO 15 FIR	39.1±3.0	0.9±0.2	0.9	39.1±3.0	0.0±0.3	0.9±0.2	0.9	350	39.1±3.0	8.9±1.0	0.039±0.007	✓
HH 211-MM	24.5±1.0	3.5±1.0	1.0	20.3±3.0	1.8±0.6	15.4±1.0	0.2	315	16.7±1.0	4.1±0.5	0.037±0.020	✓
L 1157	30.4±1.5	1.4±0.3	0.8	25.3±1.5	1.5±0.4	4.3±0.3	0.3	440	22.6±1.5	7.7±0.8	0.027±0.015	✓
IC 1396 W	30.6±2.0	1.0±0.2	1.2	30.6±2.0	0.0	1.0±0.2	1.2	750	30.6±2.0	17.0±2.0	0.073±0.010	✓
L 1211	29.8±2.0	2.3±0.6	1.6	29.8±2.0	0.0	2.3±0.6	1.6	725	29.8±2.0	33.4±4.0	0.078±0.012	✓
L 1211 FIRS2*	26.3	1.8	1.6	26.3	0.0	1.8	1.6	725	26.3	15.9	0.105	?
Cep E	41.1±3.0	1.5±0.4	0.4	35.3±3.0	0.9±0.3	3.1±0.4	0.02	730	34.4±3.0	80.4±10	0.019±0.010	✓

the method for several of our objects where sub-mm (SCUBA) and millimeter (IRAM 30-m) points from the literature were available. The obtained results are discussed for each object separately in Sect. 3.

Our best fitting results are given in Table 4 together with the fit errors. In some cases it was not possible or not useful to also do a fit for the newly detected objects in our maps, since they are at the edge of the map and so we are missing an unknown part of their flux. Some objects are detected only at the C200 wavelengths since they are outside the slightly smaller maps at the C100 wavelengths.

A determination of the fit errors cannot be obtained analytically. Therefore, we varied the PHOT measurements within their one sigma error box (five equidistant values; $S_f^m \pm n/2 \cdot \Delta S_f^m$; n = 0, 1, 2) and computed for each of the $5^4 = 625$ combinations the best fitting parameters. This results in an area of the parameter space into which the error boxes are mapped. As an example, we show in Fig. 1 this area in the (T_B,$\Sigma\Omega_B$) plane for Cep E. The errors given in Table 4 are read off such diagrams for each of our objects. The same procedure was applied also for the other parameters (L_{bol}, L_{smm}).

The determined graybody fits are then integrated to obtain the total luminosities of the sources. By integrating only at wavelengths larger than 350 μm we obtain the sub-mm luminosities L_{smm}, which can be compared to the total luminosities L_{bol} to decide whether an object is a Class 0 source (André et al. 2000). Both values, L_{bol} and L_{smm}/L_{bol}, are given in Table 4. When the ratio L_{smm}/L_{bol} exceeds 0.5%, then the object is counted as Class 0. This is equivalent to the mass ratio M_{env}/M_* being larger than unity (see André et al. 2000 and references therein). The given bolometric temperatures T_{bol} are the temperatures of a blackbody with the same luminosity as the graybody.

3. Results

Our observations of Cep E, HH 211-MM, IC 1396 W, L 1157, L 1211 and RNO 15 FIR were carried out at their nominal IRAS positions. In our ISOPHOT maps (shown in Figs. 2 – 8) we detected more objects that were actually targetted. In four cases other unexpected embedded objects or bright diffuse continuum emission are found. For L 1211 no object was detected at the nominal IRAS position, but there were two other sources discovered in the maps. The measured fluxes in all filters, including IRAS fluxes, are given in Table 3. The discrepancies of the fluxes between PSF and "aperture" photometry are for various reasons: First, it is a major problem to determine which pixel contributes to which object when doing "aperture" photometry. A second problem is the determination of the background. When using the PSF fitting method, the background is determined automatically (provided that the object is a point source and in the centre of a pixel), while for "aperture" photometry one has to choose background pixels. Concerning the absolute calibration errors for the two detectors of 15 and 10% for the C100 and C200 detector, respectively, and an additional error of 20% due to background uncertainties, we find that both flux determination methods lead to consistent results in almost all cases.

All our investigated objects are clearly of Class 0 type according to the L_{smm}/L_{bol} criterion. We cannot decide whether the newly discovered objects in our maps are of Class 0, because they are situated at the edges of the ISOPHOT maps. Due to the different sizes of the maps we certainly underestimate their fluxes at 60 and 100 μm, which alters their derived spectral energy distributions in the way that they seem to be proportionally brighter at the longer wavelengths, but to an unknown extent.

The ISOPHOT and the IRAS fluxes are consistent within the errors only for Cep E. For all other objects the IRAS point source catalogue gives values which are a factor of about 1.8 brighter. Apart from the fact that the errors for the IRAS data are quite large and in some cases only upper limits are given, the main reason for the differences is that the resolution of the IRAS satellite was not sufficient to resolve close-by sources. Only Cep E and L 1157 seem not to have other young objects in their immediate vicinity, and these are the two objects where the IRAS and ISOPHOT fluxes match the best. Cep E is a known double source (Moro-Martín et al. 2001) which cannot be resolved by IRAS nor ISOPHOT. For these reasons and the still fairly large errors in the flux measurements, no investigation of the time evolution of the fluxes of these young sources over the 14 year time span ($\approx$ 0.1% of the age of our objects) between IRAS and ISO is possible.

The PSF photometry suggests that all the objects are seen as point sources for the ISOPHOT detectors. When subtracting the fitted PSF, no systematic residuals are visible in the difference images. Thus, the angular size of the sources is at maximum 10″, a quarter of the FHWM of the PSF. This leads to an upper limit for the source solid angles of about 300 □″. This fact is supported by the inferred solid angles $\Sigma\Omega$ of $1-4\times10^{-10}$ sr (4 – 15 □″), which is less than one percent of the pixel size of the C100 detector.

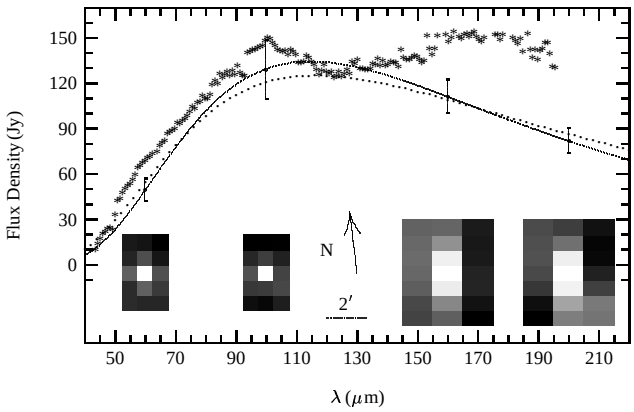

Fig. 2. ISOPHOT maps and derived photometry for Cep E. Stars (*) show the LWS spectrum, the solid line the best graybody fit (T = 35.3 K, β = 0.9, $\Sigma\Omega = 3.1\times10^{-10}$ sr) and the dotted line the best blackbody fit (T = 41.1 K, $\Sigma\Omega = 1.5\times10^{-10}$ sr) to the PHOT data. τ_{100} is 1.0. Error bars for the PHOT data only include the 15% and 10% errors of the detectors. They do not include additional uncertainties due to background determination. The four maps are centred on the central wavelength of the appropriate filter and have the same scale and orientation, given by the scale and the arrow.

For the three objects for which we obtained a LWS spectrum, we can compare the PHOT flux with the LWS continuum. While the LWS continuum is a sum of the continuum of the source and background radiation, the PHOT maps give the true flux of the source. So, the difference between LWS and PHOT should be the background radiation (e.g. from cold dust). In all three cases (Cep E, L 1157 and HH 211-MM) we clearly see evidence for such a background emission (see Figs. 2 – 5).

In the following subsections we discuss details of the results for the individual objects.

3.1. Cep E

Cep E is the brightest object in our sample. Our ISOPHOT maps at the four wavelengths of 60, 100, 160 and 200 μm are shown in the lower part of Fig. 2, all at the same scale and orientation. Photometry from these maps, and the LWS spectrum, are displayed above the maps. In addition, we plot the best-fitting graybody and blackbody fits to these data as solid and dotted lines, respectively. These fits were used to deconvolve the measurements and the filter transmission curve for converting the measured fluxes to flux densities at the central wavelengths of the used filter. For Cep E, the fluxes determined with PSF and "aperture" photometry were consistent. Deviations of the LWS continuum from the ISOPHOT data exist for wavelengths shorter than 100 and longer than 150 μm. This might be evidence for warm and cold dust. The deduced temperature is 35.3 K for the best graybody fit, which also gives $\beta = 0.9$ and $\Sigma\Omega = 3.1\times10^{-10}$ sr. On the other hand, under the assumption that the source were a perfect blackbody ($\beta = 0.0$) we deduce a temperature of 41.1 K and $\Sigma\Omega = 1.5\times10^{-10}$ sr. This fit is worse than the graybody, however. The PSF photometry shows that the object is a point source, perfectly aligned in the middle of our map, and no other embedded object is detected.

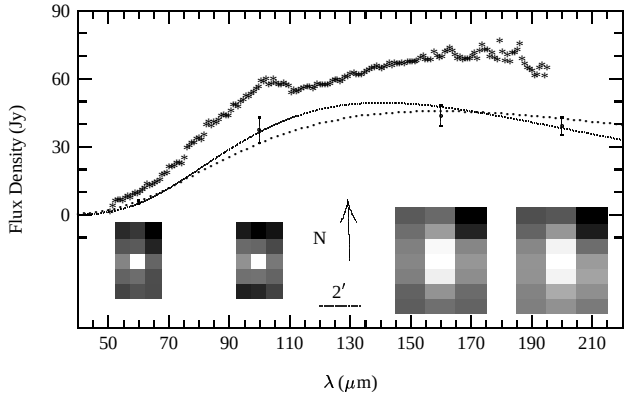

Fig. 4. As Fig. 2, but for L 1157. The best graybody has the parameters T = 25.3 K, $\beta = 1.5$, $\Sigma\Omega = 4.3\times10^{-10}$ sr and the best fitting blackbody has a temperature of T = 30.4 K and $\Sigma\Omega = 1.4\times10^{-10}$ sr.

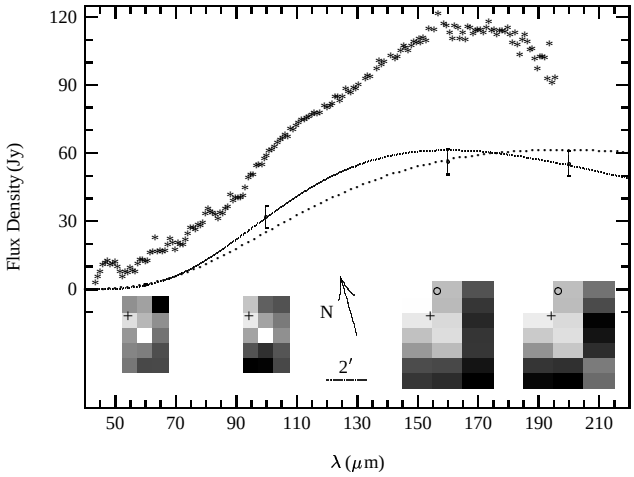

Fig. 5. As Fig. 2, but for HH 211-MM. The best graybody has the parameters T = 20.3 K, $\beta = 1.8$, $\Sigma\Omega = 15.4\times10^{-10}$ sr and the best fitting blackbody has a temperature of T = 24.5 K and $\Sigma\Omega = 3.5\times10^{-10}$ sr. The position of IC 348 IR is indicated by a + sign, and a circle marks the source IC 348 MMS, found by Eislöffel et al. (2002).

Nevertheless Cep E is at least a double source, separated by 1.4 arcseconds, as shown by the 222 GHz observations of Moro–Martín et al. (2001).

Cep E was observed by Chini et al. (2001) with SCUBA (450 and 850 μm) and the IRAM 30-m telescope (1.3 mm). They measured the fluxes in an aperture with a radius of 40″, comparable to the size of our ISOPHOT pixels and give fluxes of 43.7, 4.1 and 1.0 Jy for 450, 850 μm and 1.3 mm, respectively. When we include these values into the fit of the SED we get about the same values for the source properties: T = 34.8 K, $\beta = 1.0$ and $\Sigma\Omega = 2.8\times10^{-10}$ sr (see Fig. 3). With $rms = 2.0$ the fit is not good, mainly due to the notable deviation of the 450 μm point. This may indicate a second cold dust component in the SED. The temperature of about 35 K contradicts the value of 60 K given by Ladd and Hodapp (1997). They used the IRAS data (12, 25, 60 and 100 μm) and an 800 μm point to fit the bolometric temperature. These data do not cover the emission maximum of the source at about 160 μm (see Table 3). For an accurate determination of the temperature, however, the position of the maximum of the SED is needed.

3.2. L 1157

Our PHOT maps of L 1157, and the integrated photometry obtained from these maps, are presented in Fig. 4. This figure also shows our LWS spectrum of L 1157, as well as black and graybody fits to the photometry. L 1157 is a point source with a derived temperature of about 25.3 K, $\beta = 1.5$ and $\Sigma\Omega = 4.3\times10^{-10}$ sr. With the blackbody assumption we find a temperature of 30.4 K and $\Sigma\Omega = 1.4\times10^{-10}$ sr. There are small deviations of the LWS continuum from the PHOT photometry over the whole wavelength range. This could be due to diffuse emission from warm and cold dust, or reflecting uncertainties in the calibration of ISOPHOT. PSF photometry shows that the object is not at the centre of our map, but rather shifted slightly to the east. This could be a hint for another source nearby or a slight mispointing of the telescope due to the limited accuracy of the IRAS coordinates. Since nothing is known in the literature about a second source, we attributed all the flux to L 1157. PSF fitting to the C200 maps to confirm this was not possible, because of the unknown PSF for our half-pixel sampling in the north-south direction. Also the inferred size of the source ($\Sigma\Omega$) does not support the presence of an additional object.

L 1157 was observed with SCUBA and IRAM 30-m by Chini et al. (2001) also. They give two different measurements for the fluxes, one for the central source only (10″ aperture), and one for the source and the whole envelope (a 55″ by 30″ elliptical aperture). The fluxes are 6.0, 0.9, 0.4 Jy (source) and 25.3, 3.8, 1.3 Jy (envelope) for 450, 850 and 1300 μm, respectively. Including these fluxes (source only) to fit the SED, we get a quite good result ($rms = 0.38$) and similar values for the source properties: T = 25.3 K, $\beta = 1.6$ and $\Sigma\Omega = 4.3\times10^{-10}$ sr. If we use the fluxes for the envelope we get a much worse fit and it seems that we have a second cool component in the SED. Thus, the ISOPHOT data reflect the emission of the source itself and not the cold extended envelope.

3.3. HH 211-MM

Our PHOT maps, derived photometry and a LWS spectrum of the HH 211 region are displayed in Fig. 5. HH 211-MM at the centre of our maps is the dominant source at 60 and 100 μm. IC 348 IR, probably a heavily embedded B-star (Strom et al. 1974, McCaughrean et al. 1994), is visible to its north-east (marked by a cross). At longer wavelengths, a very cold source HH 211 FIRS2 further north becomes visible and even dominant (marked by a circle). This may be the object IC 348 MMS, found by Eisl¨offel et al. (2002) to be the source of a newly detected outflow north of HH 211. Thus, the fluxes of HH 211 FIRS2 given in Table 3 are a superposition of two different objects. The C_{60} and C_{100} measurements are dominated by IC 348 IR, while C_{160} and C_{200} are dominated by IC 348 MMS. Therefore no further investigation of the SED of one of these objects was possible.

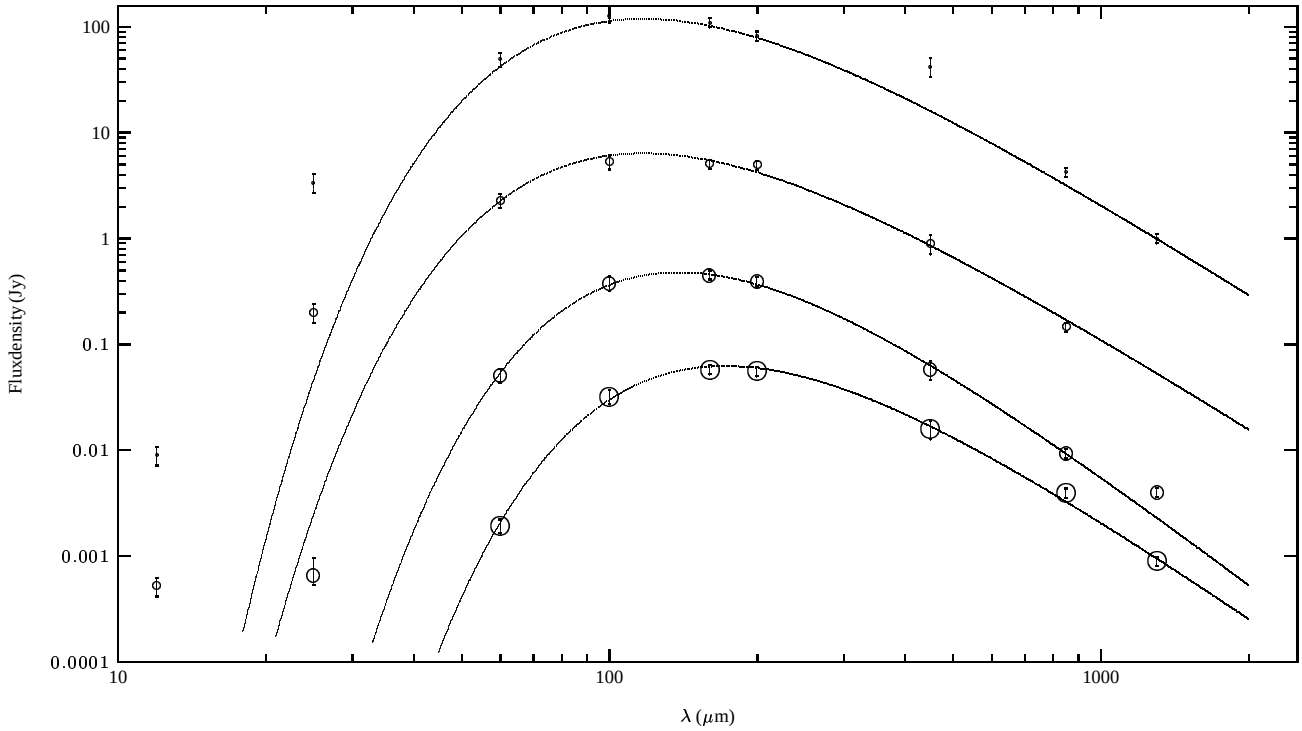

Fig. 3. Best fit using Eq. 1 and the IRAS (12 and 25 μm), ISOPHOT (60, 100, 160 and 200 μm), SCUBA (450 and 850 μm) and IRAM (1300 μm) points of Cep E, RNO 15 FIR, L 1157 and HH 211-MM (from top to bottom and from small to big circles). For obtained parameters of the best fit see text. The models and datapoints are shifted for RNO 15 FIR, L 1157 and HH 211-MM by one, two and three orders of magnitude down, respectively, for convenience. HH 211-MM was not detected by IRAS.

For HH 211-MM, we find large differences of the fluxes at 60 and 100 μm obtained with PSF and "aperture" photometry. These differences are due to the other sources influencing the background determination. In addition, there is a lot of diffuse background emission present, which can be seen in Fig. 5 as the difference between the PHOT photometry and the LWS continuum. So, it is very difficult to determine the background and to state which pixel contributes to the flux of which object. This is further complicated by the fact that HH 211 FIRS2 has a higher surface brightness than our point source HH 211-MM at 160 and 200 μm. Additionally, IC 348 IR could influence our measured flux for HH 211-MM also. Nevertheless, the derived properties for HH 211-MM are T = 20.3 K, $\beta = 1.8$, $\Sigma\Omega = 15.4\times10^{-10}$ sr for the graybody, and T = 24.5 K, $\Sigma\Omega = 3.8\times10^{-10}$ sr for the blackbody fit.

Due to the difficulties in the determination of the fluxes of HH 211-MM we supplemented the ISOPHOT data with SCUBA datapoints at 450 and 850 μm from Rengel et al. (2001) and at 1.3 mm from McCaughrean et al. (1994). The fluxes are 16.4 and 3.8 Jy for the SCUBA measurements (Rengel priv. communication) and 0.9 Jy at 1.3 mm. We find a good fit ($rms = 0.6$) and the following object parameters: T = 21.3 K, $\beta = 1.3$ and $\Sigma\Omega = 10.3\times10^{-10}$ sr. Again the inferred temperature does not differ from the value obtained from ISOPHOT data only. Due to the low temperature we find a different sub-mm slope and size of the source, since our ISOPHOT points cover only the wavelengths shortward of the emission maximum.

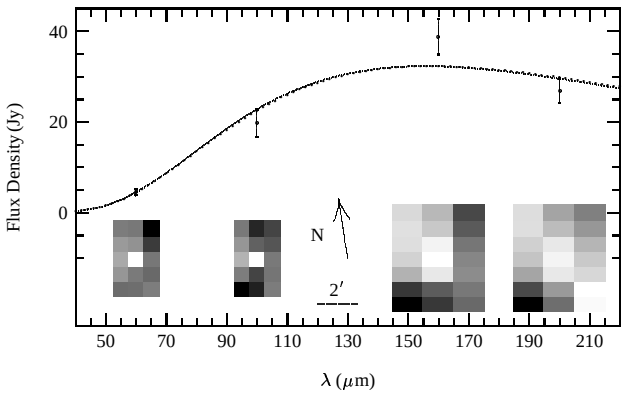

Fig. 6. As Fig. 2, but for IC 1396 W. We do not have LWS data for this source. The best graybody and blackbody fits are similar with a temperature of T = 30.6 K, $\beta = 0.0$ and $\Sigma\Omega = 1.0\times10^{-10}$ sr. A single dust component is not appropriate to fit the data. Extended cool dust, or a close group of cold sources, are seen northeast of IC 1396 W, while a very cold bright source appears at 200 μm to the south-west.

3.4. IC 1396 W

Our PHOT maps and the derived photometry for IC 1396 W are shown in Fig. 6, togther with the blackbody fit to

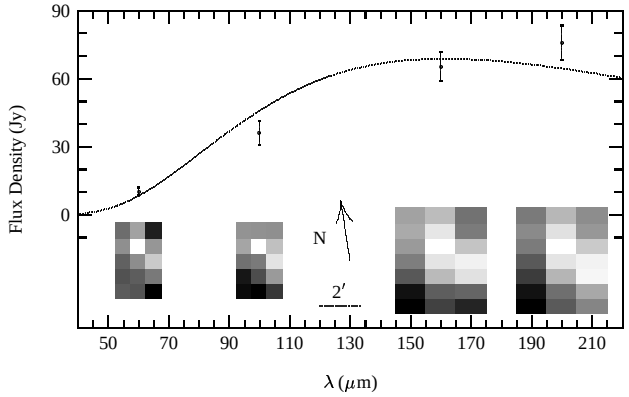

Fig. 7. As Fig. 6, but for L 1211. The best fit is a blackbody with the temperature of T = 29.8 K and $\Sigma\Omega = 2.3\times10^{-10}$ sr. Here we also have an object which is not fit well by a single dust component. The object appears north of the nominal IRAS position, and a second cool source is detected south-west of it.

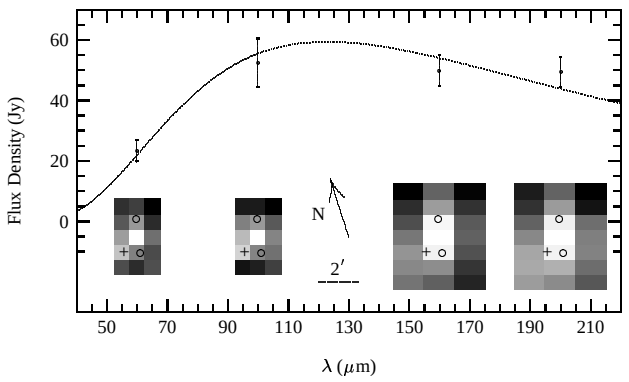

Fig. 8. As Fig. 6, but for RNO 15 FIR. The best fit is a blackbody with the temperature of T = 39.1 K and $\Sigma\Omega = 0.9\times10^{-10}$ sr. South-east of RNO 15 FIR, the warmer Class 1 source RNO 15 is detected as well (marked by a cross), especially at the shorter wavelengths. The positions of two other weak sub-mm sources (SMS1 – north, SMS2 – south) are indicated by a circle (Rengel at al. 2001, 2002).

these data. In the maps, two additional sources are evident. IC 1396 W FIRS2, to the north-east of IC 1396 W, peaks at 160 μm, whereas IC 1396 W FIRS3, to the south-west, is remarkably red, with a flux ratio at C_{200}/C_{160} of 2.6. These additional objects were not detected with the C100 detector, because the maps at these wavelengths are slightly smaller and the objects just fall outside. For IC 1396 W itself we find a temperature of T = 30.6 K, $\beta = 0.0$ and $\Sigma\Omega = 1.0\times10^{-10}$ sr for the best graybody fit. This fit is poor, however, suggesting errors in the photometry or a source with dust at more than one temperature.

3.5. L 1211

Our PHOT maps of L 1211, the derived photometry, and a blackbody fit to these data are displayed in Fig. 7. Somewhat to our surprise, the L 1211 source was not found at its nominal IRAS position, but is shifted a full pixel, corresponding to 45″ to the north. A second source L 1211 FIRS2, is found in the south-west. The best fits to both sources are blackbodys with temperatures of T = 29.8 K and T = 26.3 K for L 1211 and L 1211 FIRS2, respectively. We infer a solid angle $\Sigma\Omega$ of the sources of 2.3 and 1.8×10^{-10} sr. The quality of these fits is not good (the rms is 1.6), as in the case of RNO 15 FIR. Comparing our maps with the work of Tafalla et al. (1999) and Anglada & Rodríguez (2002) we find that our object L 1211 is identical to MMS 4 or VLA 5 and the object L 1211 FIRS2 seems to be a superposition of MMS 3, MMS 2 and MMS 1, and VLA 3 and VLA 1, respectively.

Tafalla et al. (1999) classify L 1211 as a transitional object between Class 0 and Class 1. They use the IRAS fluxes and an additional observation at 1.2 mm (0.135 Jy). With these data, as for our ISO data, the maximum of the emission could not be determined exactly. It could only be constrained to lie between 100 and 1200 μm. With our ISO data, we could corroborate the assumption that L 1211 is of Class 0, since the maximum of the SED is at $\lambda > 160\,\mu$m. If we use the 1.2 mm datapoint from Tafalla et al. (1999) for our analysis, we get quite a bad fit with $rms = 3$, which may be indicating a large amount of cold dust in the envelope of this source.

3.6. RNO 15 FIR

The ISOPHOT maps of the RNO 15 FIR region are shown in Fig. 8, together with the derived photometry and the blackbody fit to these data. Visible on our maps are RNO 15 FIR in the centre, and the Class 1 source RNO 15 to the south-east, marked by a cross. Since this source is warmer than RNO 15 FIR, it is seen well at the shorter wavelengths, but fades considerably relative to RNO 15 FIR towards the longer wavelengths. From higher spatial resolution sub-mm maps at 450 and 850 μm taken with SCUBA (Rengel et al. 2002) we know that two other emission objects SMS1 and SMS2 are present to the north and south of RNO 15 FIR, but are merged with it at ISOPHOT resolution. They surely influence our flux measurements, so that the inferred properties for RNO 15 FIR (T = 39.1 K and $\Sigma\Omega = 0.9\times10^{-10}$ sr) have larger uncertainties.

Since the ISOPHOT measurements show a broad and not well defined maximum of the SED, we supplement these data with SCUBA measurements of Rengel et al. (2001) to determine more accurate source properties. The fluxes at 450 and 850 μm are measured in a 45″ by 45″ aperture and are 9.2 and 1.4 Jy (Rengel priv. communication). Using these data in combination with the ISOPHOT points we get slightly different values for the temperature and the size of the source (T = 34.8 K, $\Sigma\Omega = 1.5\times10^{-10}$ sr) and the sub-mm slope is $\beta = 1.0$. The quality of the fit with $rms = 0.96$ is not good. This may be due to the fact that RNO 15 FIR is a double source, as suggested by Davis et al. (1997). It is also indicated by the deviation of the data points from the determined SED (see Fig. 3).

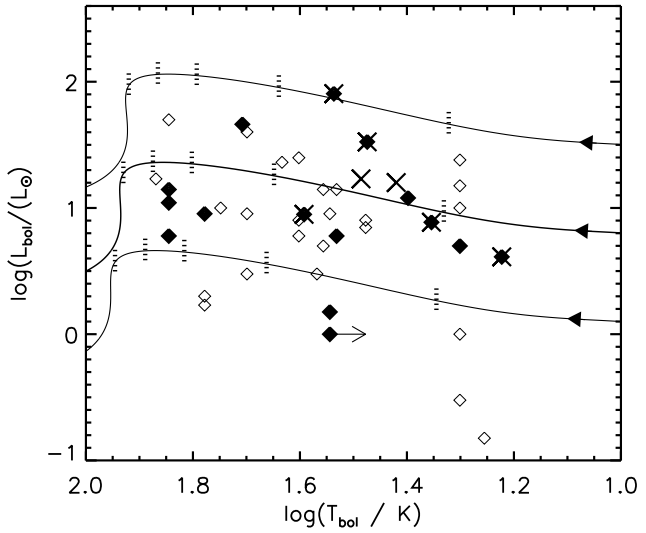

Fig. 9. The bolometric luminosity–temperature diagram for the Class 0 data analysed here (thick Xs), the Class 0 data from Table 5 (filled diamonds) and the Class 0 data from the review of Andr´e et al. (2000) (open diamonds). The superimposed evolutionary tracks are discussed in Section 5. Protostars evolve from right to left. Three tracks for final masses of 0.2, 1 and 5 $M_\odot$ are displayed. The model peak accretion rate is reached at 17,000 yr, and the power law fall-off is $\propto t^{-7/4}$ with time t, on a 30,000 yr timescale. The vertical dotted lines on the tracks mark the model ages of 20,30 40, 50 and 75 thousand years.

Table 5. Summary of the Class 0 sources for which a correlation of the source properties with the outflow luminosity in the 1 – 0 S(1) line of H_2 was investigated. Except for our objects observed with ISOPHOT, L_{bol} and T_{bol} are adapted from Andr´e et al. (2000), as well as all the M_{env} values. The outflow luminosities are either from published literature or our own measurements. In the Ref. column the references are given where we took $L_{H_2\ 1-0\,S(1)}$ measurements from.

Object	L_{bol} [$L_\odot$]	T_{bol} [K]	M_{env} [$M_\odot$]	$L_{H_2\ 1-0\,S(1)}$ [$10^{-3}\,L_\odot$]	Ref.
RNO 15 FIR	8.9	39.1	–	0.46	1, 6
HH 211-MM	4.1	16.7	1.5	3.1	2, 6
L 1157	7.7	22.6	0.5	6.1	3, 6
L 1211	33.4	29.8	–	10.7	6
Cep E	80.4	34.4	7.0	70.0	4, 6
L 1448 N	11.0	70.0	2.3	2.16	6
L 1448 IRS2	6.0	70 ?	0.9	2.8	6
L 1448 C	9.0	60.0	1.4	5.7	6
IRAS 03282	1.5	35.0	0.6	4.46	6
HH 212 MM	14.0	70 ?	1.2	5.3	5, 6
HH 24 MMS	5.0	20 ?	4.0	1.21	1, 6
HH 25 MMS	6.0	34.0	0.5	6.61	1
NGC 2264 G VLA2	12.0	25.0	2.0	7.75	3
VLA 1623	1.0	<35	0.7	0.81	3, 6
Ser – FIRS1	46.0	51.0	3.0	0.64	6

References: (1) Davis et al. (1997) (2) McCaughrean et al. (1994) (3) Davis & Eislöffel (1995) (4) Eislöffel et al. (1996) (5) Zinnecker et al. (1998) (6) own measurements

4. Discussion

4.1. Mass and Age determination

Do Class 0 objects develop into Class 1 and Class 2 protostars? To answer this, we wish to determine basic parameters for the Class 0 protostars, such as age, surrounding mass, present mass and final mass. These, however, are model dependent quantities. In Fig. 9 we plot the locations of our seven (including L 1211 FIRS2) sources on the $L_{bol} - T_{bol}$ diagram (large crosses), which is the protostellar equivalent of a Hertzsprung-Russell diagram (Myers et al. 1998). Also plotted on the diagram are the data for another 37 Class 0 protostars, as listed by André et al. (2000). Two of these sources possess bolometric luminosities above 1000 $L_\odot$, and so fall outside the display. Note that Class 0 protostars possess bolometric temperatures below ~ 80 K.

The present sample contains quite powerful and cold Class 0 members. Two sources lie above the location of the other explored sources. These are L 1211 and Cep E. As we demonstrate below, such powerful Class 0 sources with low bolometric temperature, can indeed be included in an evolutionary model through the Classes 0 – 1 – 2. The large surrounding masses observed restrict the type of model and these objects could go on to produce high-mass stars.

The model tracks plotted represent the evolution of three protostars which end up accumulating masses of 0.2, 1 and 5 $M_\odot$. The tracks were derived by combining the Unification Scheme, as reviewed by Smith (2000, 2002), with the framework for protostellar envelopes presented by Myers et al. (1998), according to the prescription presented below. We thus determine model ages, present masses of the protostellar nucleus, envelope masses and the final stellar masses (Table 6). The result is that the more massive Class 0 protostars possess large envelopes and would become massive stars. According to the model described here, most of the envelope, however, is not accreted but dispersed, if the majority of protostars here are to form low-mass stars. Note that alternative schemes have been presented by Bontemps et al. 1995, Saraceno et al. 1996 and André 2000.

4.2. Outflow Luminosity vs. Source Properties

Is the luminosity of the outflows from the Class 0 sources correlated with the properties of the sources like their bolometric luminosity, the temperature or mass of their envelopes? To answer this question we measured the luminosity of the outflows from 15 of the Class 0 sources in André et al. (2000) and our objects, in the 1 – 0 S(1) line of molecular hydrogen at 2.122 μm. Due to the short cooling times (some years, Smith and Brand (1990)), H_2 is a good tracer of emission of shocked gas caused by current interactions between outflowing material and the surrounding gas. The 1 – 0 S(1) line of H_2 is usually the brightest ro-vibrational line in a spectrum of shocked gas and thus most easily detected.

In magnetohydrodynamic models of Class 0 sources (e.g. Shu et al. (1994), Hirose et al. (1997) and Ouyed and Pudritz (1997)) the accretion rate onto the protostar is connected to the

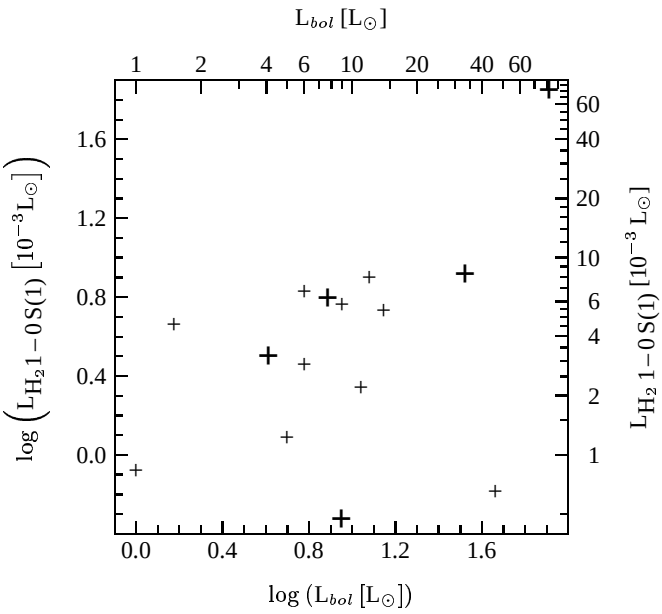

Fig. 10. Measured outflow luminosity in the 1 – 0 S(1) line of H_2 versus the bolometric source luminosity for the sources listed in Table 5. The objects investigated in this paper are marked with a large + sign. No significant correlation is found for this sample.

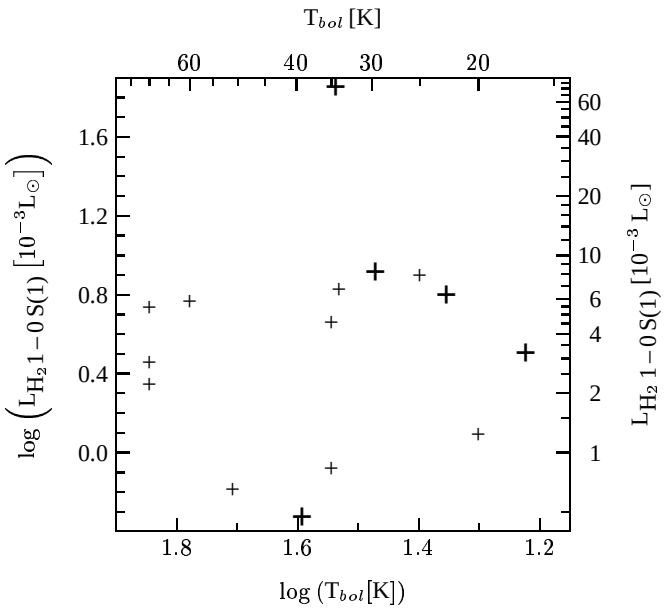

Fig. 11. As Fig. 10 but for the bolometric temperatures of the Class 0 sources from Table 5. No significant correlation is found for this sample.

amount of material injected into the outfbwing jet. This material interacts with the surrounding quiescent gas in shocks. Hence, the luminosity of these shocks may be connected to the mass accretion rate and thus to the source properties. Here, we tested for correlations of the 1 – 0 S(1) H_2 luminosity with the source bolometric luminosity, the bolometric temperature and the mass of the surrounding protostellar envelope given by André et al. (2000). The results of these comparisons are shown in Figs. 10, 11 and 12. We obtained a linear regression for each case and tested if the slope of the regression line differed statistically signifi cantly from a slope value of zero. With a probability of error of 5 % none of the regression lines differs from a constant value. Additionally a Kolmogorow-Smirnow-Test shows, that with a probability of error of 0.1 % the data is not consistent with a constant value. Thus, a signifi cant correlation of the outfbw luminosity in the 1 – 0 S(1) line of H_2 with any source parameter was not found.

The lack of such correlations may have various explanations. For example, in each outfbw, we observe H_2 emission at various distances from the source and these knots or bow shocks are indicating material which was ejected from the source at different times in the past (Δt = distance to the source/jet velocity). Also, the knot luminosity depends on the local properties of the surrounding gas (e.g. gas density, atomic fraction). Additionally, the extinction gradient in the K-band along the outfbw is not known. It will alter the measured relative and total fluxes in the sense that knots closer to the source appear fainter due to higher extinction. In Section 5, however, we argue that the location on these diagrams depends sensitively on both mass and age, which results in a wide scatter. Therefore, the lack of a signifi cant correlation of the present source properties and the outfbw luminosity in the H_2 1 – 0 S(1) line may not be surprising.

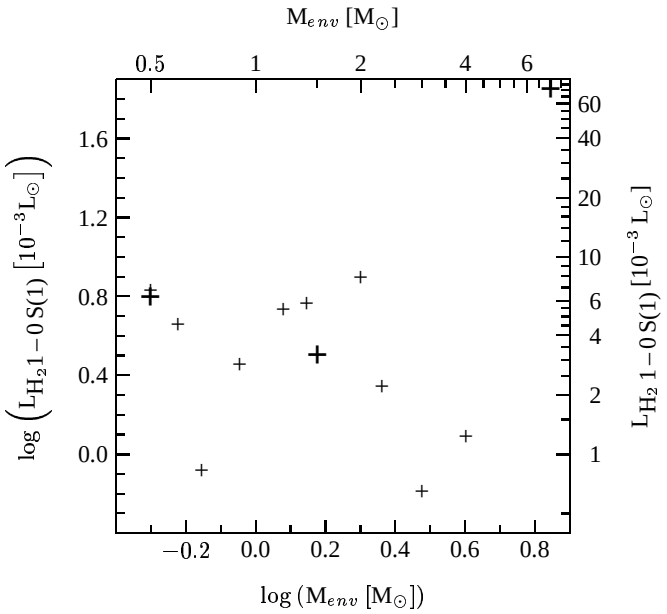

Fig. 12. As Fig. 10 but for the envelope masses of the Class 0 sources from Table 5. For RNO 15 FIR and L 1211, we do not have measurements of the envelope mass. No significant correlation is found for this sample.

A better tool for comparing the outfbws to source properties may be an optically thin line of CO (e.g. the 1 – 0 ^{13}CO line), which should give a measurement of the time-integrated power of the outfbw without being influenced by local extinction effects. Comparable observations in the same transition and isotope of CO are needed for a statistically reasonable sample of objects to study their behaviour. At present, only small samples of Class 0 sources have been thus analysed (e.g. Bontemps et al. 1995; Smith 2000, 2002).

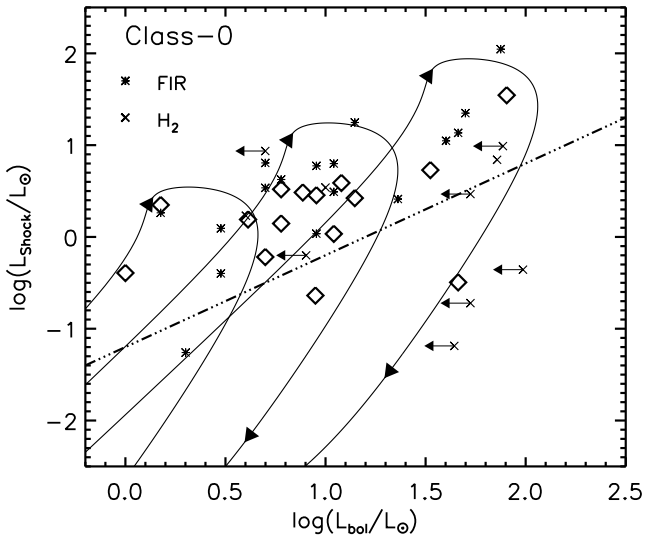

Fig. 13. The derived outflow shock luminosity versus the bolometric source luminosity for the Class 0 sources listed in Table 5, as well as the Class 0 sample investigatd by Stanke (2000) (symbol: 'x') and the far-infrared line ISO luminosities presented by Giannini et al. (2001) (symbol: '*'). The model tracks are for the same three models presented in Fig 9 and the straight line divides model Class 0 and model Class 1 protostars, as determined by the protostar possessing half of its final mass.

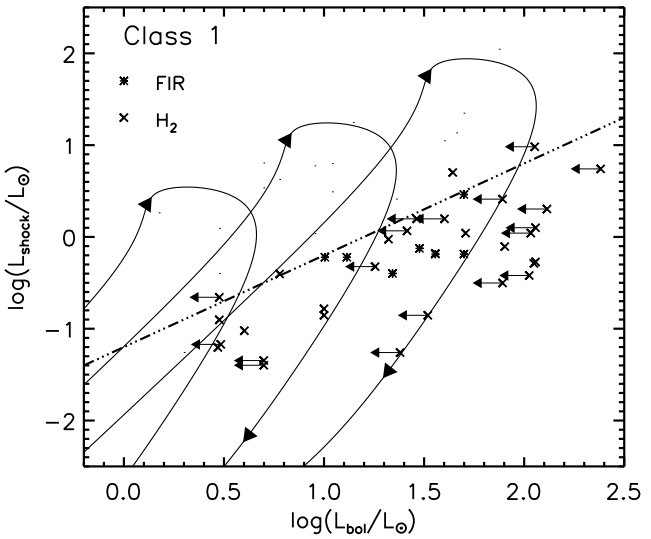

Fig. 14. The derived outflow shock luminosity versus the bolometric source luminosity for Class 1 sources from the sample of Stanke (2000) (symbol: 'x') and the far-infrared line ISO luminosities presented by Giannini et al. (2001) (symbol: '*'). The model tracks are for the same three models presented in Fig 9 and the straight line divides model Class 0 and model Class 1 protostars, as determined by the protostar possessing half of its final mass.

5. An evolutionary scheme

An evolutionary model for protostars is presented in the Appendix. The outflow scheme has been elaborated by Smith (1999, 2000, 2002) and applied by Davis et al. (1998), Yu et al. (2000) and Stanke et al. (2000). It is based on a prescribed accretion rate from an envelope. Modelling of outflows has demonstrated that the fraction of mass which escapes through jets must reach a maximum during the Class 0 stage. This is required to account for the excess momentum and power of Class 0 bipolar outflows, as calculated from observations of emission lines of CO rotational transitions (see Smith 2000). We outline in the Appendix the fundamental formula of the evolutionary scheme.

According to previous modelling of the envelope, three parameters must be introduced to generate plausible models for the bolometric temperature. As shown by Myers et al. (1998), these are (1) the envelope's outer temperature (here $T_o = 24$ K), (2) the efficiency of accretion of the envelope into the star-jet system and (3) the difference in evolutionary timescale between the envelope and the protostar. The envelope consists of material which will fall onto the central object as well as mass directly lost soon after the Class 0 stage. This extra mass component proves necessary to produce a low bolometric temperature, as observed for the Class 0 sources, yet must be rapidly lost in order to yield T Tauri stars within a reasonable time (Myers et al. 1998).

Previously, we modelled the envelope evolution by assuming mass conservation. Here, we find two significant adjustments are necessary in order to model the new data and maintain plausible time scales. First, the initial mass in the envelope which will eventually fall inwards is reduced to 87% of the total required mass to form the star and excavate the bipolar outflow. The other 13 % is presumed to initially lie within a flattened disk. This yields the values in the column 'infall mass' in Table 6.

In Fig. 9, we plot the sample summarised in Table 5 for Class 0 sources for which a correlation of the source properties with the outflow luminosity in the 1 – 0 S(1) line of H_2 has been investigated. Note that this sample includes warmer and less luminous protostars than in the ISOPHOT sample investigated above. According to the tracks, this corresponds to a wide range in final stellar masses. The lowest mass star forming here is found to be VLA 1623 (assuming $T_{bol} = 35$ K) which will reach just 0.07 $M_\odot$, owing to its low bolometric luminosity of only 1 $L_\odot$ (André et al. 2000). The low final mass is a result of this version of the evolutionary scheme employed, for which we maintain the same accretion timescale but alter the accretion rate to generate the tracks. This implies that the final mass is nearly proportional to the peak accretion luminosity. Future statistical studies will lead to revisions of this first model. be able to revise the scheme.

The simplest form of the unifying model, assumed here, is that a fraction of the jet power is instantaneously dissipated in shock waves, while the bipolar outflow is a time-averaged recording of the momentum outflow. To model the outflow, we have previously employed the H_2 luminosity, $L(H_2)$, which we estimate to be ten times the 1 – 0 S(1) luminosity. This is consistent with expectations from shock physics and allows a comparison with previous diagrams presented by Stanke (2000) and Smith (2002). Here, however, we shall use the jet power itself as the comparison parameter. For the comparison, we assume that the observed emission is produced in the warm shocks where the jets dissipate their energy, L_{shock}.

Table 6. Parameters derived for the seven objects from the model evolutions. The minimum mass is the total mass with density distributed as $\rho \propto r^{-3/2}$ necessary to provide an optically thick sphere out to a radius R_{bol}, corresponding to the observed T_{bol}. The infall mass is the envelope mass which remains to be accreted (a part of which will escape in the jets), and the envelope mass is the total mass predicted on projecting the distribution out to a radius corresponding to the chosen ambient temperature of 24 K. The model mass accretion rate decreases as $t^{-7/4}$ on a 30,000 yr timescale. The age is given in years, the masses are in solar masses.

Object	Age	Mass	Final mass	Min. mass	Infall mass	Env. mass
RNO 15 FIR	27000	0.10	0.5	0.10	0.37	1.4
HH 211-MM	17100	0.06	0.6	6.67	0.47	7.2
L 1157	20000	0.12	0.9	2.03	0.68	5.9
IC 1396 W	24000	0.22	1.3	0.83	0.99	5.5
L 1211	23000	0.40	2.5	1.77	1.85	10.7
L 1211 FIRS2	22000	0.20	1.3	1.48	1.02	6.9
Cep E	26000	0.96	5.2	1.64	3.71	16.3

The fraction of the jet power dissipated in molecular hydrogen lines is taken to be 2 %. This is consistent with numerical simulations and bow shock modelling which predict, typically, 10 % of the infrared radiation from shocks in dense clouds to be in the form of H_2 lines. We also assume that 80 % of the jet energy is hidden by just under two magnitudes of K-band extinction. The shock power has also been estimated from the far-infrared lines of CO, OI, OH and H_2O, measured by ISO (Giannini et al. 2001). Here, we shall assume that these lines in total, within the ISO-LWS beam, also represent 2 % of the jet power, L_{shock}. We thus increase estimated H_2 and sub-mm luminosities by 50 to yield the displayed values. While these approximations are far from ideal, they permit us to determine if the evolutionary scheme is plausible.

Figure 13 demonstrates that the Class 0 protostars possess almost exclusively high ratios of $L(H_{shock})/L_{bol}$ (one of the two sources well within the Class 1 regime is VLA 1623 which may be obscured by up to 5 magnitudes of K-band extinction; see Davis & Eisl¨offel 1995). Furthermore, these data are consistent with the same model tracks fitted to the bolometric luminosity–temperature data. The lack of a correlation in the data is thus put down to the combination of the distributions in both mass and age.

In addition, previously measured Class 1 outflows almost all lie below the predicted Class border line, as shown in Fig. 14. Note, however, that for many of the H_2 flows in Orion detected by Stanke (2000) only upper limits for the bolometric luminosity are available. Nevertheless, the division of the two Classes with the model straight line where the protostar has acquired half the final stellar mass, is evident.

Figures 15 demonstrates that the model is also consistent with the envelope properties. The main exceptions apparent from this diagram are a group of low luminosity H_2 objects. This suggests that the extinction for these sources may far exceed the fiducial two magnitudes.

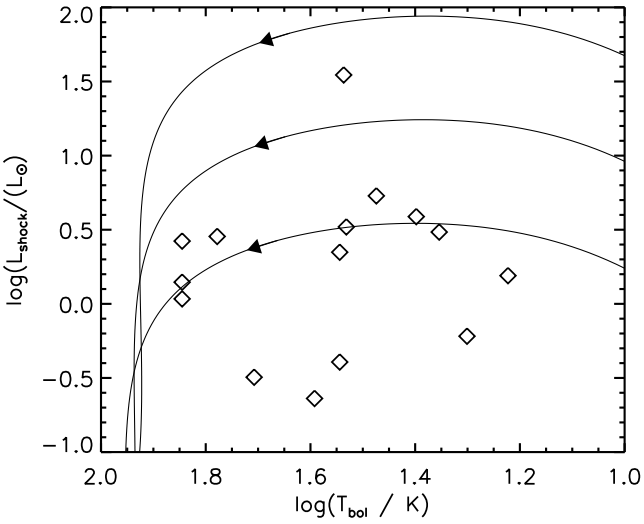

Fig. 15. The derived outflow shock luminosity versus the bolometric source temperature for the Class 0 sources listed in Table 5. The model tracks are for the same three models presented in Fig 9.

6. Conclusions

We have determined the spectral energy distributions for the six deeply embedded objects Cep E, L 1211, IC 1396 W, L 1157, HH 211-MM and RNO 15 FIR in the far-infrared with ISO. The inferred temperatures and L_{smm}/L_{bol} ratios confirm their Class 0 nature, within the errors. Employing an evolutionary scheme, we are able to determine the age, surrounding mass and the current and final mass of these sources. Two of them, Cep E and L 1211 seem to become intermediate mass stars, while the others will develop into solar mass stars or lower mass objects. The comparison of the ISOPHOT and LWS observations for three of the sources reveals the existense of emission from cold dust in the immediate vicinity of the objects.

A comparison of the luminosity in the 1 – 0 S(1) line of H_2 of the related outflows for 15 Class 0 sources, with the source bolometric luminosity, bolometric temperature and envelope mass was done. We found no statistically significant correlation of the outflow luminosity with each of these source parameters. This could be due to the H_2 luminosity mainly depending on the local properties of the surrounding gas.

The unifying scheme, however, explains the lack of correlations as due to evolutionary effects. Furthermore, the scheme which involves a redistribution of mass between envelope, disk, protostar, jets and outflow, accounts for the differences in source properties according to the Class.

Acknowledgements. Jochen Eislöffel and Dirk Froebrich received financial support from the DLR through Verbundforschung grant 50 OR 9904 9.

We thank Manfred Stickel from MPIA for his help with the data reduction of the PHOT data.

We would like to thank the referee Dr. P.M. Andr´e for his very useful comments, which helped to clarify and improve the readability of the paper.

We also thank Alex Rosen for a critical reading of the manuscript and the Department of Culture, Arts and Leisure, Northern Ireland for financial support.

The ISOPHOT data presented in this paper were reduced using PIA, which is a joint development by the ESA Astrophysics Division and the ISOPHOT Consortium with the collaboration of the Infrared Processing and Analysis Center (IPAC). Contributing ISOPHOT Consortium institutes are DIAS, RAL, AIP, MPIK and MPIA.
The ISO Spectral Analysis Package (ISAP) is a joint development by the LWS and SWS Instrument Teams and Data Centers. Contributing institutes are CESR, IAS, IPAC, MPE, RAL and SRON.

Appendix

We present and test a model based on the transfer of gas between components. We take a spherical envelope of gas and dust, and prescribe an accretion rate from the inner edge of the envelope onto a disk. Note that we assume a centrifugal barrier at 30 AU, which defines the inner envelope – outer disc transition. The accretion disk processes most of the mass onto the protostar and a fraction into twin jets. The speed of the jets is assumed to be a fixed fraction of the escape speed from the protostellar surface.

The accretion rate from the envelope is taken to increase exponentially for a short period before decreasing as a power law through the Class 0, 1 and 2 phases. The zero point of time is thus defined as the moment when accretion starts and, simultaneously, a central hydrostatic object forms. The accretion rate is

$$\dot{M}_a(t) = \dot{M}_o(e/\alpha)^{\alpha}(t/t_o)^{-\alpha}\exp(-t_o/t). \quad (5)$$

Energy release through accretion and contraction are included. In the models shown, the peak accretion rate is reached at $t_o/\alpha = 17,000$ yr, and the power law index is $\alpha = 7/4$, on a t_o = 30,000 yr timescale. The accreted mass is predominantly accrued by the growing protostars. The fraction $\epsilon(t)$ which escapes through twin jets reaches a maximum of $\eta = 0.2$ at the peak accretion time:

$$\epsilon = \eta \left[\frac{\dot{M}_a(t)}{\dot{M}_o}\right]^{\zeta} \quad (6)$$

where $\zeta = 2$ is found to be appropriate. Hence the mass left over, which accretes onto the core to form the star is

$$M_*(t) = \int_0^t (1 - \epsilon)\,\dot{M}_a. \quad (7)$$

To form a star like the Sun, this model will provide an early accretion peak in which $\dot{M}_a \sim 10^{-4} M_\odot\,\mathrm{yr}^{-1}$ for 10^4 years, and eventually becoming $\dot{M}_a \sim 10^{-7} M_\odot\,\mathrm{yr}^{-1}$ for 10^6 years, corresponding to Class 0 and Class 2 or Classical T Tauri stars, respectively. The power-law has substantial observational support (Calvet et al. 2000).

We previously modelled the envelope evolution by assuming mass conservation. Here, we make two significant adjustments in order to model the new data. First, the initial mass in the envelope which will eventually fall inwards is reduced to 87% of the total required mass to form the star and excavate the bipolar outflow. The other 13 % is presumed to initially lie within a flattened disk. This yields the values in the column 'infall mass' in Table 6. The total mass can be written analytically in terms of an incomplete Gamma function on integrating Eqn. 5:

$$M_{infall}(t) = \dot{M}_o t_o (e/\alpha)^{\alpha}\left[1 - \Gamma(\alpha - 1, t_o/t)\right]. \quad (8)$$

Secondly, we find that the low bolometric temperatures of Class 0 protostars can only be attained by introducing an additional mass component to the envelope. In confirmation of the results of Myers et al. (1998), we find that this extra mass is lost on a shorter timescale than the protostellar accretion timescale. The bolometric temperature is calculated according to the optically thick case of Myers et al. (1998). We thus extend the opacity law approximation employed up to 60 to 120 μm with the same form and take the optically thick envelope throughout the early evolutionary stages. We have thus found here that an envelope mass

$$M_{env}(t) = M_{inf} \cdot (0.87 + \mu(t/t_o)^{-2\alpha}) \quad (9)$$

where $\mu = 2$ provides bolometric temperatures, timescales and masses consistent with the observed samples.

The envelope mass provides a testable prediction. This mass is not strongly dependent on the evolutionary path but is necessary to provide the optical depth out to a sufficiently large radius to permit the measured low bolometric temperature. The total mass is dominated by the outer regions of the envelope, while the total optical depth is controlled by the inner region (for all plausible density distributions such as $\rho \propto r^{-3/2}$, as assumed here). Hence, the mass is sensitive to the extent of the envelope. For this reason, we present three determinations of the envelope mass in Table 6. Masses derived from submillimetre observations yield quite low extended masses (André et al. 2000), consistent with the absence of more mass than necessary to form the star and feed the jets (Smith 2000). It is clear that both the observationally derived mass and model mass are sensitive to chosen physical parameters and both will need refining.

References

Andr´e, P., Ward-Thompson, D., Barsony, M. 2000, in Protostars and Planets IV, 59
Anglada, G., Rodr´ıguez, L.F., 2002, Revista Mexicana de Astronom´ıa y Astrof´ısica, 38, 12
Bontemps, S., Andr´e P., Terebey S., Cabrit S., 1996, A&A, 311, 858
Calvet N., Hartmann L.W., Strom S.E., 2000, in Protostars & Planets IV, ed. V. Mannings et al., (Tucson, U. of Arizona Press), 377
Chini, R., Ward-Thompson, D., Kirk, J.M., Nielbock, M., Reipurth, B., Sievers, A., 2001, A&A, 369, 155
Clegg, P.E., Ade, P.A.R., Armand, C., et al., 1996, A&A, 315, L38
Davis, C.J., Eislöffel, J., 1995, A&A, 300, 851
Davis C.J., Smith M.D., Moriarty-Schieven G.H., 1998, MNRAS, 299, 825
Davis, C.J., Ray, T.P., Eislöffel, J., Corcoran, D., 1997, A&A, 324, 263
Eislöffel, J., Froebrich, D., Stanke, T., McCaughrean, M.J., 2002, in prep.
Eislöffel, J., Smith, M.D., Davis, C.J., Ray, T.P., 1996, AJ, 112, 2086
Gabriel, C., et al., 1997, in ASP Conf. Ser. Vol. 125, Astronomical Data Analysis Software and Systems (ADASS) VI, ed. G. Hunt & H.E. Payne, (San Francisco ASP), 108

Giannini, T., Nisini, B., Lorenzetti, D., 2001, ApJ, 555, 40
Gueth, F., Guilloteau, S., 1999, A&A, 343, 571
Gueth, F., Guilloteau, S., Dutrey, A., Bachiller, R., 1997, A&A, 323, 943
Hirose, S., Uchida, Y., Shibata, K., Matsumoto, R., 1997, PASJ, 49, 193
Kessler, M.F., Steinz, J.A., Anderegg, M.E., et al., 1996, A&A, 315, L27
Ladd, E.F., Hodapp, K.-W., 1997, ApJ, 475, 749
Laureijs, R.J., 1999, Point spread function fractions related to the ISOPHOT C100 and C200 arrays, ISO-Data centre, Astrophysics Division, ESA, Villafranca Spain, http://www.iso.vilspa.esa.es/users/expl_lib/PHT/c200fpsf02.ps.gz
Lefloch, B., Eislöffel, J., Lazareff, B., 1996, A&A, 313, L17
Lemke, D., Klaas, U., Abolins, J., et al., 1996, A&A, 315, L64
McCaughrean, M.J., Rayner, J.T., Zinnecker, H., 1994, AJ, 436, L189
Moro-Mart´ın, A., Noriega-Crespo, A., Molinari, S., Testi, L., Chernicharo, J., Sargent, A. 2001, A&A, 555, 146
Motte, F., Andr´e, P., 2001, A&A, 365, 440
Myers, P.C., Adams, F.C., Chen, H., Schaff, E., 1998, ApJ, 492, 703
Ouyed, R., Pudritz, R.E., 1997, ApJ, 482, 712
Rengel, M., Froebrich, D., Eislöffel, J., Hodapp, K., 2001, AG Abstr. Ser. 18, 66
Rengel, M., Froebrich, D., Hodapp, K., Eislöffel, J., 2002, In: The Origins of Stars and Planets: The VLT View, João Alves & Mark McCaughrean (ed.)
Saraceno P., Andr´e P., Ceccarelli C., Griffin M., Molinari S., 1996, A&A 309 827
Shu, F., Najita, J., Ostriker, E., Wilkin, F., Ruden, S., Lizano, S., 1994, ApJ, 429, 781
Smith M.D., 1999, Astrophysics and Space Science, 261, 169
Smith, M.D., 2000, IAJ, 25, 27
Smith, M.D., 2002, In: The Origins of Stars and Planets: The VLT View, João Alves & Mark McCaughrean (ed.)
Smith, M.D., Brand, P.W.J.L., 1990, MNRAS, 245, 108
Stanke, T., 2000, Ph.D. thesis (AIP, Potsdam)
Strom, S.E., Strom, K.A., Carrasco, L., 1974, PASP, 86, 798
Tafalla, M., Myers, P.C., Mardones, D., Bachiller, R., 1999, A&A, 348, 479
Yu, K.C., Billawala, Y., Smith, M.D., Bally, J., Butner, H., 2000, AJ, 120, 1974
Zinnecker, H., McCaughrean, M.J., Rayner, J.T., 1998, Nature, 394, 862